Nanophotonic coherent imager

Firooz Aflatouni,[1,2,*] **Behrooz Abiri,**[1] **Angad Rekhi,**[1] **and Ali Hajimiri**[1]

[1]*Department of Electrical Engineering, California Institute of Technology, Pasadena, CA 91125, USA*

[2]*Department of Electrical and Systems Engineering, University of Pennsylvania, Philadelphia, PA 19104, USA*

[*]*firooz@seas.upenn.edu*

Abstract: An integrated silicon nanophotonic coherent imager (NCI), with a 4×4 array of coherent pixels is reported. In the proposed NCI, on-chip optical processing determines the intensity and depth of each point on the imaged object based on the instantaneous phase and amplitude of the optical wave incident on each pixel. The NCI operates based on a modified time-domain frequency modulated continuous wave (FMCW) ranging scheme, where concurrent time-domain measurements of both period and the zero-crossing time of each electrical output of the nanophotonic chip allows the NCI to overcome the traditional resolution limits of frequency domain detection. The detection of both intensity and relative delay enables applications such as high-resolution 3D reflective and transmissive imaging as well as index contrast imaging. We demonstrate 3D imaging with $15\mu m$ depth resolution and $50\mu m$ lateral resolution (limited by the pixel spacing) at up to 0.5-meter range. The reported NCI is also capable of detecting a 1% equivalent refractive index contrast at 1mm thickness.

OCIS codes: (110.1650) Coherence imaging; (110.6880) Three-dimensional image acquisition; (280.3640) Lidar.

References and links

1. A. Kirmani, D. Venkatraman, D. Shin, A. Colao, F. N. C. Wong, J. H. Shapiro, and V. K. Goyal, "First-photon imaging," Science **343**(6166), 58-61 (2013).
2. A. McCarthy, X. Ren, A. D. Frera, N. R. Gemmell, N. J. Krichel, C. Scarcella, A. Ruggeri, A. Tosi, and G. S. Buller, "Kilometer-range depth imaging at 1550 nm wavelength using an InGaAs/InP single-photon avalanche diode detector," Opt. Express **21**(19), 22098-22113 (2013).
3. M. D. Learmouth, "High resolution laser lidar utilizing two-section distributed feedback semiconductor laser as a coherent source," Electron. Lett. **26**(9), 577-579 (1990).
4. S. Gao and R. Hui, "Frequency-modulated continuous-wave lidar using I/Q modulator for simplified heterodyne detection," Optics Letters **37**(11), 2022-2024 (2012).
5. J. Busck and H. Heiselberg, "Gated viewing and high-accuracy three-dimensional laser radar," Appl. Opt. **43**(24), 4705-4710 (2004).
6. R. M. Marino, T. Stephens, R. E. Hatch, J. L. McLaughlin, J. G. Mooney, M. E. O'Brien, G. S. Rowe, J. S. Adams, L. Skelly, R. C. Knowlton, S. E. Forman, and W. R. Davis, "A compact 3D imaging laser radar system using Geiger-mode APD arrays: system and measurements," Proc. SPIE **5086**, 1-15 (2003).
7. D. P. Hutchinson, "Coherent infrared imaging camera," Proc. SPIE **2540**, 204-209 (1998).
8. M. Hochberg and T. Baehr-Jones, "Towards fabless silicon photonics," Nature Photon. **4**, 492-494 (2010).
9. B. Abiri, F. Aflatouni, A. Rekhi, and A. Hajimiri, "Electronic two-dimensional beam steering for integrated optical phased arrays," Optical Fiber Communication Conference (OFC), paper M2K.7 (2014).
10. F. Aflatouni and H. Hashemi, "An electronically controlled semiconductor laser phased array," International Microwave Symposium Digest (IMS), 1-3 (2012).
11. J. Sun, E. Timurdogan, A. Yaacobi, E. Shah Hosseini, and M. R. Watts, "Large-scale nanophotonic phased array," Nature **493**(7431), 195-199 (2013).

#228915 - $15.00 USD Received 8 Dec 2014; revised 29 Jan 2015; accepted 30 Jan 2015; published 19 Feb 2015

12. M. Izutsu, Y. Nakai, and T. Sueta, "Operation mechanism of the single-mode optical-waveguide Y junction," Opt. Lett. **7**(3), 136-138 (1982).
13. K. W. Ang, T. Y. Liow, Q. Fang, Jun-F.Song,Y. Z. Xiong, M. B. Yu, G. O. Lo, and D. L. Kwong, "Low thermal budget monolithic integration of evanescent-coupled Ge-on-SOI photodetector on Si CMOS platform," IEEE J. Sel. Top. Quantum Electron. **16**(1), 106-113 (2010).
14. A. Novack, Y. Liu, R. Ding, M. Gould, T. Baehr-Jones, Q. Li, Y. Yang, Y. Ma, Y. Zhang, K. Padmaraju, K. Bergmen, A. E. J. Lim, G. Q. Lo, and M. Hochberg, "A 30 GHz silicon photonic platform," in proc. SPIE **8781** (2013).
15. I. V. Komarov and S. M. Smolskiy, *Fundamentals of short-range FM radar* (Artech House, 2003).

1. Introduction

Three-dimensional (3D) imaging has many applications in bio-medical imaging, nano-particle characterization, security, robotics, and gesture recognition. Although 3D imaging systems have been studied, they are usually realized either as single pixel detectors [1–4] or as bench-top systems with simple detector arrays [5–7]. Silicon nanophotonic processes use similar steps as their electronic counterparts, leading to higher yields, and compatibility with electronic integrated circuits. This combined with the low loss and high confinement of silicon waveguides [8] make the silicon photonics an ideal platform for coherent 3D imaging and projection systems [9–11] with high resolution and pixel count.

Infrared (IR) optical electromagnetic waves are promising candidates for high-resolution 3D imaging due to their short wavelength. These wavelengths can be processed efficiently by integrated silicon-on-insulator (SOI) nanophotonic platforms with high confinement and relatively low loss. A recent demonstration of phased array transmitters [9, 11] is an example of the advantage of SOI platforms in implementing complex nanophotonic systems. The high fabrication yields and potential for integration with silicon electronics necessary for additional signal processing make SOI nanophotonic processes a suitable platform for realization of NCIs with large number of pixels in a small area at low cost.

In this paper we report a nanophotonic coherent imager that uses an array of integrated silicon photonics antennas to couple the impinging infrared electromagnetic wave into a series of nanophotonic waveguides, which coherently process the optical signals to measure the instantaneous phase and amplitude of the incident wave on each pixel to form a 3D image of the target object. An electrically generated frequency chirp is used to produce a linearly chirped optical wave that illuminates the object. A part of this optical signal serves as a reference and is coherently combined with the received signal by each pixel on the silicon nanophotonic chip to produce an electrical output. The proposed NCI uses time-domain signal detection and processing of this electrical output to resolve the relative phase and power of the incident wave at each pixel. This simultaneously enables high depth resolution and large dynamic range, overcoming some of the limitations of conventional frequency domain FMCW approaches. The NCI chip can be used in 3D reflective, transmissive, and index contrast imaging modes with a high spatial resolution of about $15\mu m$ over a large dynamic range of 0.5m without use of a wide range highly linear tunable laser source. To our knowledge, this is the first coherent imager that enables multiple phase sensitive imaging schemes via a single nanophotonic chip.

2. Coherent imager architecture

The structure of the 4×4 NCI is depicted in Fig. 1. A part of the laser output that is used to illuminate the target object being imaged is coupled into the input grating coupler through an optical fiber and then is guided to a Y-junction splitter network through silicon nano-waveguides. This coupled coherent light, the reference signal, is split into 16 equal intensity optical signals. The incoming light from the object is coupled into nano-waveguides through an array of grating couplers [8] serving as pixels. The received light from each pixel is then combined with a

#228915 - $15.00 USD Received 8 Dec 2014; revised 29 Jan 2015; accepted 30 Jan 2015; published 19 Feb 2015

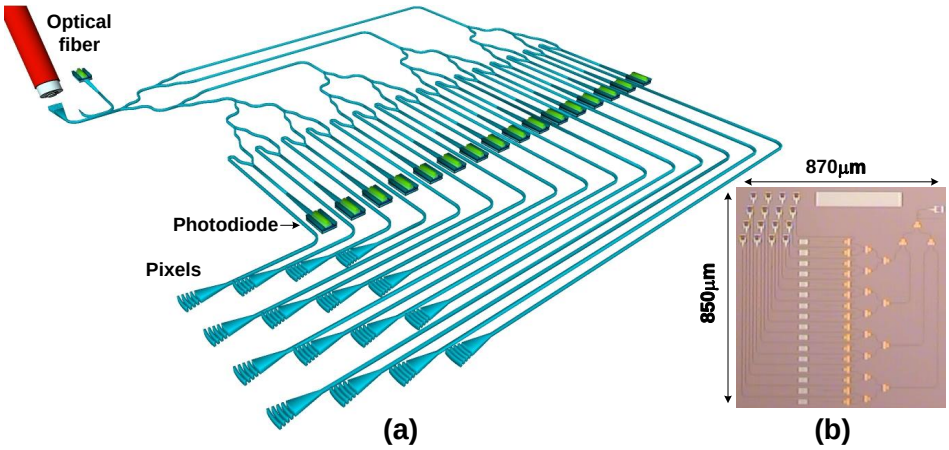

Fig. 1. (a) The structure of the 4×4 NCI, in which the light coming from the object is collected using 16 grating couplers (pixels) is shown. A fraction of the coherent light that is used to illuminate the object is guided using an optical fiber and is coupled into the chip through a grating coupler. This coupled light is combined with the collected optical signals from the object and is photo-detected using on-chip silicon-germanium photodiodes. (b) The NCI micro-photograph implemented on standard IME silicon-on-insulator process.

part of the reference signal in a Y-junction combiner [12] and is converted to electrical current using a silicon-germanium photo-detector [13]. Figure 1(b) shows the NCI micro-photograph implemented on IME SOI photonic process [14]. The implemented NCI can be used in the transmissive, reflective, and index contrast imaging modes.

2.1. Theory of operation

Figure 2(a) shows the imaging system for i^{th} grating coupler. The output electric field of the laser emitting with power P_0 at angular frequency ω_0 is represented by $E_L(t) = \sqrt{P_0}e^{j\omega_0 t}$. The laser output is intensity modulated with a frequency-chirped electrical voltage $v(t)$ using a Mach-Zehnder modulator (MZM). The use of an electrically generated frequency chirp eliminates the need for a tunable laser source with highly linear chirp response. An erbium-doped fiber amplifier (EDFA) is placed after the modulator. The parameter G accounts for the gain of the EDFA and the loss of the MZM. The EDFA output is split into two branches using a fiber optic fusion coupler. The light in the top branch is collimated and used as the illumination source. Part of the light coming from the target object is coupled into the NCI chip by the i^{th} grating coupler. The light in the bottom branch, the reference signal, is also coupled into the NCI chip. The coupled reference signal is split into 16 branches and combined with the signal from the i^{th} grading coupler in a Y-junction. The Y-junction output is then photo-detected and the photo-current $i(t)$ is wire-bonded to the electronic circuit. The grating coupler efficiency and the on-chip waveguide loss in the top branch are represented by γ, while β accounts for the excess loss of the 1-to-16 on-chip splitter and the grating coupler efficiency. The total delay difference between the top and the bottom arms, τ_0, consists of the delay in the optical fiber, τ_{of}, and the free-space delay, τ_f. As shown in Fig. 2(a), in the transmissive mode, the target object which is substantially transparent at the operating wavelength is placed between the collimator and the grating coupler. In this case, τ_f increases as the light slows down in the target object. In the reflective mode, the light is reflected from the object and forms an image on the pixel array (not shown). For this case, τ_f contains information on the spatial depth of the target object.

#228915 - $15.00 USD Received 8 Dec 2014; revised 29 Jan 2015; accepted 30 Jan 2015; published 19 Feb 2015

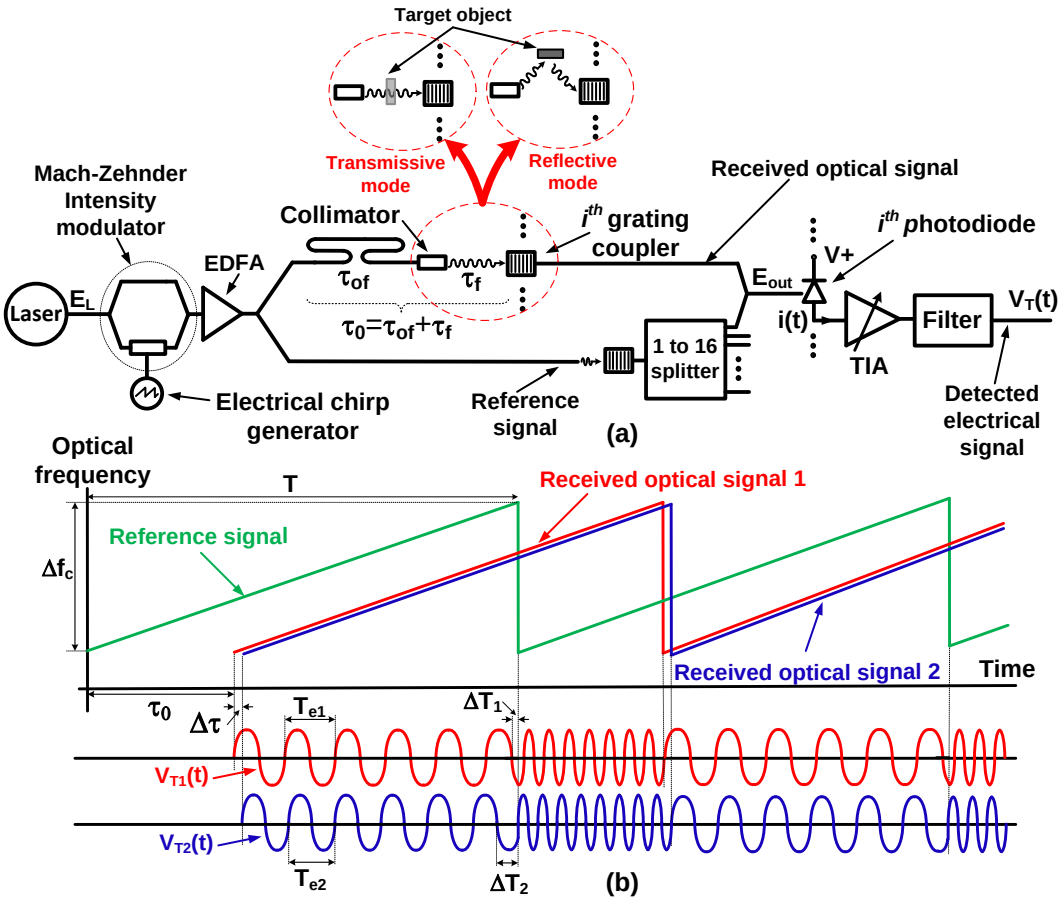

Fig. 2. (a) Simplified block diagram of the imaging system for one pixel (grating coupler) is shown. (b) The optical and electrical signals at different points of the imager are depicted. The number of zero crossings per chirp period is used as a coarse estimate for the delay difference between the top arm and the bottom arm. The time difference between the last zero crossing in $V_{T1}(t)$ and $V_{T2}(t)$ and the end of the frequency ramp is used to find the fine estimate for the relative delay between two arms.

In order to study the principle of operation of the imager, it is useful to consider the case that the collimator is directly illuminating the pixel array and therefore, τ_f represents the free space delay and depends on the distance between the collimator and the pixel array. In this case, the electric field of the combined signal, E_{out}, can be written as

$$E_{out} = \frac{\sqrt{GP_0}}{4} e^{j\omega_0 t}[\sqrt{\beta}(1+e^{j\frac{v(t)}{V_\pi}\pi}) + \gamma e^{-j\phi}(1+e^{j\frac{v(t-\tau_0)}{V_\pi}\pi})], \quad (1)$$

where V_π and ϕ are the MZM gain and the optical phase difference between the top and the bottom arms at the combining point, respectively. The electrical voltage $v(t)$ represents an electrical linear frequency-chirped signal and can be written as

$$v(t) = a_0 cos(\omega_e t + 2\pi\alpha t^2), \quad (2)$$

where a_0, ω_e, and α, are the amplitude, the starting point of the electrical frequency chirp, and the frequency chirp rate in $[\frac{Hz}{s}]$, respectively. Substituting Eq. (2) into Eq. (1) and using the

#228915 - $15.00 USD Received 8 Dec 2014; revised 29 Jan 2015; accepted 30 Jan 2015; published 19 Feb 2015

Jacobi-Anger expansion (*i.e.,* $e^{jzcos(\theta)} = \sum_{k=-\infty}^{\infty}(j)^k J_k(z)e^{jk\theta}$), the DC and AC components of the photodiode current can be written as

$$i_{AC}(t) = \frac{1}{4}RP_0G\sqrt{\beta\gamma}cos(\phi)\sum_{n=1}^{\infty}J_n^2(\frac{a_0}{V_\pi}\pi)cos(4n\pi\tau_0\alpha t + n\omega_e\tau_0 - 2n\pi\alpha\tau_0^2), \tag{3}$$

$$i_{DC} = \frac{1}{8}RP_0G(\beta+\gamma+\sqrt{\beta\gamma}J_0^2(\frac{a_0}{V_\pi}\pi)cos(\phi)), \tag{4}$$

where R is the photodiode responsivity and J_n represents the Bessel function of the first kind. The photodiode current is amplified and converted to a voltage using an off-chip trans-impedance amplifier (TIA) with adjustable gain. Considering only the fundamental component, the output voltage, $V_T(t)$, can be written as

$$V_T(t) = \frac{1}{4}K_{TIA}RP_0G\sqrt{\beta\gamma}J_1^2(\frac{a_0}{V_\pi}\pi)cos(\phi)cos(4\pi\tau_0\alpha t + \omega_e\tau_0 - 2\pi\alpha\tau_0^2), \tag{5}$$

where K_{TIA} is the controllable gain of the TIA. Equation 5 shows that the frequency of the detected signal is a linear function of the delay difference between the received signal and the optical reference signal. This detection scheme is similar to that of a FMCW radar [15], since the optical reference signal and the detected signal at each pixel will be at different optical frequencies due to the difference in their propagation delays. Therefore, different time delays between the reference signal and the receive signal at each pixel results in different electrical frequencies detected at corresponding photodiode of the NCI chip.

Defining the frequency sweep range, $\Delta f_c = \alpha T$, and using Eq. (5) the period of $V_T(t)$ can be calculated as

$$T_e = \frac{T}{2\tau_0\Delta f_c}, \tag{6}$$

where T is the chirp period. Two cases are studied in Fig. 2(b). In case 1, the total delay difference between top and bottom arms in Fig. 2(a) is set to τ_0. In case 2, the distance between the collimator and the i^{th} grating coupler of the NCI is slightly increased, such that this total delay difference increases to $\tau_0+\Delta\tau$. For case 1 and case 2, electrical signals $V_{T1}(t)$ and $V_{T2}(t)$ with different frequencies appear at the output of the filter, respectively. By knowing the chirp rate α and counting the number of zero crossings in V_{T1} or V_{T2}, a coarse estimate for the delay difference τ_0 can be achieved. However, the amount of the small delay difference between cases 1 and 2, $\Delta\tau$, can not be estimated by counting the number of zero crossings of V_{T1} or V_{T2}. In order to find a fine estimate for $\Delta\tau$, the time difference between the last zero crossing in $V_{T1}(t)$ and $V_{T2}(t)$ and the end of the frequency ramp (*i.e.,* ΔT_1 and ΔT_2) can be used. First, from Fig. 2(b) the chirp period, T, can be written in terms of the periods of V_{T1} and V_{T2} as

$$T = \tau_0 + NT_{e1} + \Delta T_1 = \tau_0 + \Delta\tau + NT_{e2} + \Delta T_2, \tag{7}$$

where N represents the number of full periods of $V_{T1}(t)$ or $V_{T2}(t)$ that appears within the chirp period T. In this case, assuming $\Delta\tau \ll \tau_0$, the difference between ΔT_1 and ΔT_2 can be calculated as

$$\Delta T_2 - \Delta T_1 = N(T_{e1} - T_{e2}). \tag{8}$$

Using Eq. (6) the difference between the periods of $V_{T1}(t)$ and $V_{T2}(t)$ can be written as

$$T_{e1} - T_{e2} = \frac{T}{2\Delta f_c}(\frac{1}{\tau_0} - \frac{1}{\tau_0+\Delta\tau}) \overset{\Delta\tau \ll \tau_0}{\approx} \frac{T}{2\Delta f_c}(\frac{\Delta\tau}{\tau_0^2}). \tag{9}$$

#228915 - $15.00 USD Received 8 Dec 2014; revised 29 Jan 2015; accepted 30 Jan 2015; published 19 Feb 2015

Also, from Fig. 2(b), $N = \frac{T-\tau_0}{T_{e1}}$ is calculated. In practice, τ_0 is much smaller than the chirp period T and hence, $N = \frac{T}{T_{e1}}$ is assumed which together with Eqs. (6), (8), and (9) can be used to find $\Delta\tau$ as

$$\Delta\tau = \frac{\tau_0}{T}(\Delta T_2 - \Delta T_1). \tag{10}$$

Therefore, the minimum detectable delay or the delay resolution is written as

$$\Delta\tau_{min} = \frac{\tau_0}{T}(\Delta T_2 - \Delta T_1)_{min}, \tag{11}$$

where $(\Delta T_2 - \Delta T_1)_{min}$ is the minimum detectable value for $(\Delta T_2 - \Delta T_1)$ which is mainly limited by the total timing jitter of the detected electrical signal. This total timing jitter depends on the timing jitter of the electronic detection system, the timing jitter of the electrical chirp generator, and the signal-to-noise ratio (SNR) at the input of the electronic detection system. Note that $\Delta\tau_{min}$ sets the imaging resolution in all NCI modes of operation as it defines the smallest detectable thickness for a given refractive index in transmissive mode, the smallest detectable refractive index variations for a given thickness in index contrast imaging mode, and the depth resolution in reflective mode. For example, defining the depth resolution in free space as $\Delta x_{min} = \frac{1}{2}C_0\Delta\tau_{min}$ in reflective mode, for a $(\Delta T_2 - \Delta T_1)_{min}$ of $5ns$, $\tau_0 = 5ns$, and $T = 0.5ms$, a depth resolution of $\Delta x_{min} = 7.5\mu m$ can be achieved. The factor of $\frac{1}{2}$ is added to account for half of the round-trip delay in the reflective mode. Also note that even if the number of zero crossings for $V_{T1}(t)$ and $V_{T2}(t)$ are not the same within the chirp period, T, the aforementioned $\Delta\tau_{min}$ calculation can be used for fine resolution detection, as the electrical receiver measures T_{e1} and T_{e2} accurately and accounts for different number of zero crossings per chirp period for $V_{T1}(t)$ and $V_{T2}(t)$.

One important challenge in the implemented NCI is that the phase difference between the top and bottom arms in Fig. 2(a), ϕ, may vary slowly with time due to the presence of a thermal gradient between two arms. This results in a slow amplitude fluctuation for the detected signal as Eq. (3) suggests. However, the DC component of the photo-current in Eq. (4) also experiences the same thermal fluctuation and is used to form a phase correction loop by placing a thermal phase modulator on the optical reference signal path. This feedback loop together with an automatic gain control (AGC) loop in electronic detection circuit keeps the amplitude of the detected electrical signal constant. Also, note that the variations in the term $(\omega_e\tau_0 - 2\pi\alpha\tau_0^2)$ in Eq. (5) are negligible compared to ΔT_1 (or ΔT_2) and do not affect the performance of the reported imager.

2.2. Transmissive imaging mode

The block diagram of the transmissive measurement setup is illustrated in Fig. 3(a). A laser source is intensity modulated with a frequency-chirped electrical signal. In transmissive imaging mode, the collimated beam passes through the object and impinges on the NCI chip. The generated photo-current resulting from beating the reference optical signal and the received signal by each pixel is amplified using an array of TIAs, filtered, and captured by the detection system. In this mode, the object being imaged is substantially transparent at the laser operating wavelength. The object is placed between the collimator and the NCI chip. In this mode, a motorized micro-positioner moves the object by equivalently 16-pixel increments to emulate a larger pixel array. At each position, different parts of the collimated beam that are passing through the parts of the object with different spatial depths experience different time delays when arriving at the corresponding pixels of the NCI chip.

As discussed in section 2.1, the coarse spatial depth of the object being imaged is automatically calculated by counting the number of zero-crossings per chirp period and the fine

#228915 - $15.00 USD Received 8 Dec 2014; revised 29 Jan 2015; accepted 30 Jan 2015; published 19 Feb 2015

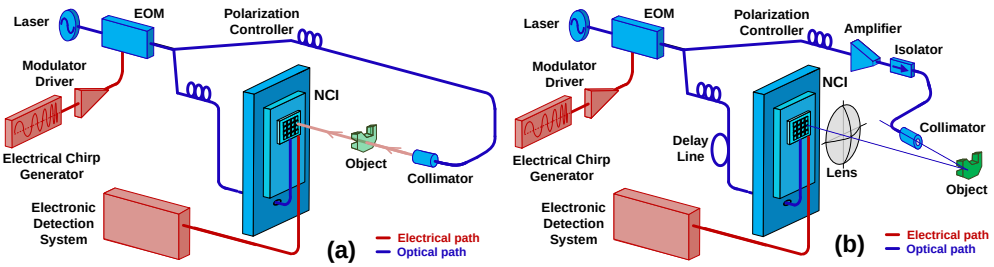

Fig. 3. (a) The block diagram of the transmissive measurement setup using integrated NCI is shown. The collimated infrared beam passes through the substantially transparent object (at the operating wavelength) and is collected by the 16 pixels of the imager. The collected optical signal is combined with the reference signal, a fraction of the coherent source output used for illuminating the object, and is photo-detected. The photo-current is then directed to the electronic detection system. (b) The block diagram of the reflective mode measurement setup is depicted. The amplified output of the coherent source is collimated and is used to illuminate the object. A lens is used to form an image on the NCI pixel array.

spatial depth of the object is calculated by measuring the time difference between the last zero-crossing in one chirp period to the end of the chirp period. By combining these coarse and fine depth detection schemes, a very fine depth resolution over a large spatial dynamic range can be achieved.

2.3. Reflective imaging mode

In the reflective measurement setup, a collimator is used to coherently illuminate the object and the image is formed on the pixel array using a lens, as depicted in Fig. 3(b). The detection scheme is identical to that of the transmissive mode. However, the optical power at the output of the collimator is increased to improve the signal-to-noise ratio at the input of the electronic detection system. In this mode, to emulate a larger pixel array, the pixel array is moved using an automated micro-positioner with increments of 4×4 pixels while keeping the lens stationary.

3. Measurement results

The NCIs were fabricated in IME silicon-on-insulator technology node [14] where silicon-on-insulator wafers with a $0.22\mu m$ top silicon layer and $2\mu m$ buried oxide are used. Three levels of silicon etching were available. The pixels are lensed grating couplers with effective area of $17\mu m \times 17\mu m$ and with 40% average coupling efficiency that were designed using two levels of etching. Travelling wave photodiodes were designed based on epitaxial growth of germanium on top of silicon waveguides and have measured responsivity of 0.7A/W. An average optical loss of 1.8dB/cm for a 500nm wide and 220nm thick silicon waveguide was measured. Two aluminum metal layers with thickness less than $1.5\mu m$ were available. No post processing was done on the fabricated chips. The fabricated chips were mounted on a printed circuit board (PCB) and electrically connected to the PCB using bond wires while the optical fiber carrying the reference optical signal was attached to the reference grating coupler. No temperature control was required. All measurements have been carried out at the room-temperature.

For all measurements, a laser source emitting at λ_0=1.55μm is intensity modulated with a frequency-chirped electrical signal. The frequency of the electrical signal increases linearly with time from 1MHz to 3.8GHz, over $500\mu s$, periodically. To measure the minimum depth resolution in the transmissive mode, first the collimator output power is set to 10mW. In this case

#228915 - $15.00 USD Received 8 Dec 2014; revised 29 Jan 2015; accepted 30 Jan 2015; published 19 Feb 2015

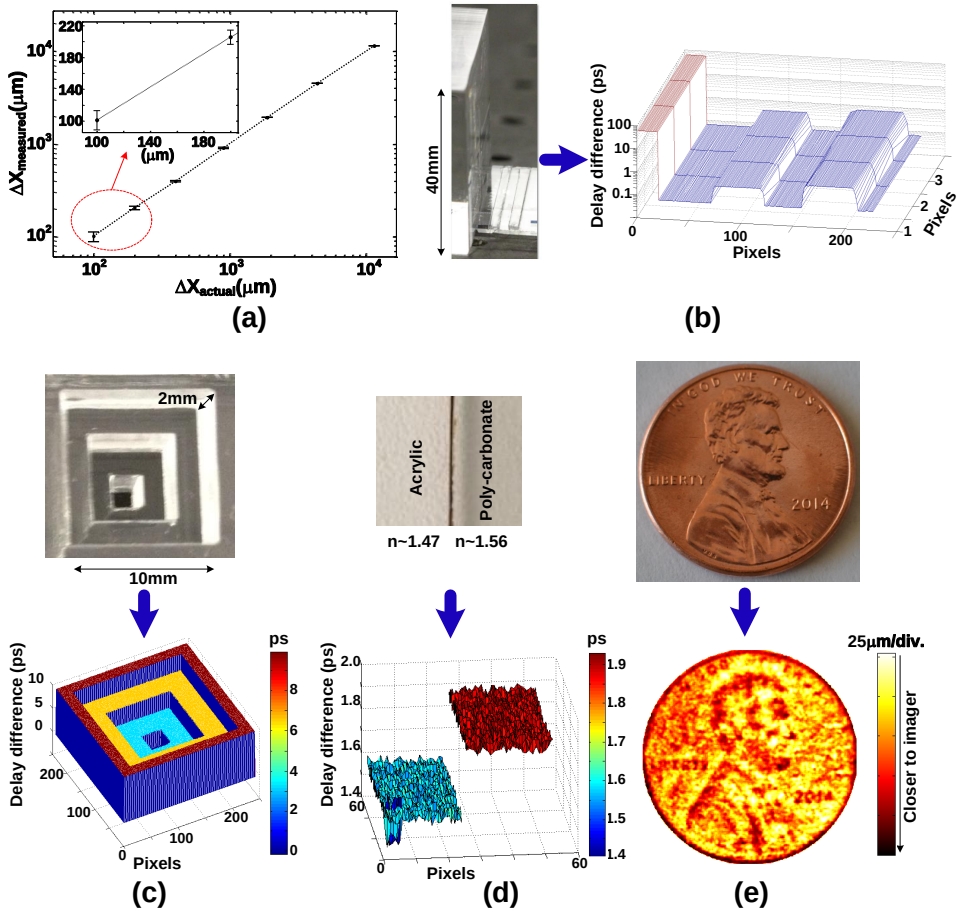

Fig. 4. (a) The measured distance vs. actual distance in μm for transmissive mode is shown. (b) The concurrent high depth resolution and large dynamic range offered by the integrated NCI in the transmissive mode is demonstrated. A 4cm object and two small pedestals with sub-$100\mu m$ depth difference are concurrently imaged (left: the object, right: the 3D image). (c) The transmissive 3D image of a transparent pyramid is shown (top: the object, bottom: the 3D image). (d) The index of refraction contrast imaging using integrated NCI is demonstrated; top: two materials with the same thickness, bottom: the index contrast image. (e) The depth image of the US one-cent coin taken using the integrated NCI in the reflective mode is shown. The measured free-space relative propagation delay corresponding to the image depth is represented by pixel colors; pixels represented by dark red are closer to the imager. The image is approximately extended over $140\mu m$ of spatial depth.

each grating coupler receives about $4\mu W$. Then, the free-space distance between the collimator and the NCI is changed using the motorized micro-positioner. For each position, 10 measurements per pixel were conducted. The measured distance vs. actual distance is depicted in Fig. 4(a). The error bars on this graph represent the range of all 160 measurements for each distance setting. The highest range of error occurs for the $100\mu m$ distance measurements (shown as an inset) where a $15\mu m$ deviation from the actual value can be observed corresponding to a $15\mu m$ depth resolution. This depth resolution is in close agreement with the predicted value from Eq.

#228915 - $15.00 USD Received 8 Dec 2014; revised 29 Jan 2015; accepted 30 Jan 2015; published 19 Feb 2015

(11), for $(\Delta T_2 - \Delta T_1)_{min} \approx 5ns$, $\tau_0 \approx 5ns$, and $T = 0.5ms$.

In a different experiment, a 40mm thick Plexiglas cube was placed next to two small pedestals with approximate thickness of $150\mu m$ and $225\mu m$, respectively (Fig. 4(b)-left). The 3D transmissive image shown in Fig. 4(b)-right demonstrates that a high spatial resolution over a large dynamic range can be achieved with a single measurement and without modifying the measurement setup and parameters. In another experiment, the 3D transmissive image of a hollow pyramid made of Plexiglas (Fig. 4(c)-top) was formed which is depicted in Fig. 4(c)-bottom. For all transmissive measurements, the output power of the collimator is set to 10mW. Due to scattering from abrupt edges of the target object, the SNR of the received signal at corresponding pixel may be reduced significantly resulting in inaccurate zero-crossing detection. To avoid this uncertainty, the pixels with low SNR are tagged automatically during the imaging stage and in the post-processing stage, their values are automatically replaced by the average of the surrounding pixels. Figure 4(d) shows the refractive index contrast imaging that is conducted using the transmissive imaging setup. In Fig. 4(d)-top, a sheet of Polycarbonate with typical index of 1.56 is placed next to a sheet of Plexiglas with typical index of 1.47. Both sheets have thickness of 1mm. The image in Fig. 4(d)-bottom shows a clear difference in the detected thickness corresponding to the contrast in the index of refractions of two materials.

In reflective mode measurements, the collimator output power is set to $120mW$ and each pixel receives about $0.2\mu W$ in presence of the lens. Fig. 4(e)-bottom shows the reflective depth image of a US one-cent coin (in Fig. 4(e)-top) where in the setup in Fig. 3(c), a micro-positioner is used to move the 4×4 NCI with increments of 4×4 pixels (without moving the lens) to mimic a larger coherent pixel array. The 3D image in Fig. 4(e)-bottom has a depth resolution of about $15\mu m$ and lateral resolution of $50\mu m$ limited by the on-chip pixel spacing.

4. Conclusion

We have demonstrated a nanophotonic coherent imager implemented on a silicon photonics platform where all optical signal processing and detection is done on a single photonic chip. Use of low-cost and robust silicon photonics platform combined with modified FMCW detection scheme enables 3D imaging with high depth resolution of $15\mu m$ over a large dynamic range of 0.5m. Using the implemented integrated NCI, we have conducted high resolution index of refraction contrast imaging, 3D transmissive, and 3D reflective imaging. Use of silicon photonics platform enables realization of NCIs with large number of pixels making low-cost high performance NCIs available for varieties of applications in near future.

Acknowledgments

We thank OpSIS foundry for the fabrication of the chips and Profs. Micheal Hochberg and Tom Baehr-Jones from University of Delaware for valuable discussions on the fabrication process.